Performance Comparison of Quadcopters with Variable-RPM and Variable-Pitch Rotors

Michael McKay
PhD Student

Robert Niemiec
PhD Candidate

Farhan Gandhi
Redfern Chair in Aerospace Engineering

Rotorcraft Adaptive and Morphing Structures Laboratory
Department of Mechanical, Aerospace and Nuclear Engineering
Rensselaer Polytechnic Institute
Troy, NY, United States

ABSTRACT

Use of variable-pitch rotors was compared against variable-RPM rotors on a 2kg (20N) quadcopter. To generate 5N of thrust in hover while maintaining a 2:1 maximum thrust-to-weight ratio, the variable-pitch rotor required 29% more power. At low climb rates the variable-RPM rotor requires less power, but near its maximum rate it required more power than the variable-pitch rotor. The maximum climb rate for the variable-pitch rotor was up to 70% greater than the variable-RPM rotor. A quadcopter equipped with variable-pitch rotors required more power to operate compared to the aircraft with variable-RPM rotors over its operational airspeed range. The variable-pitch quadcopter required 30% more power at best-endurance speed, and had 18% less range than the variable-RPM quadcopter (at maximum-range speed). The 1/ rev root drag shear was 42% larger for the variable-RPM rotor, and the 2/rev H- and Y-forces were 37% and 50% larger. The 2/rev thrust vibration was 6.5% smaller for the variable-RPM rotor, and the hub pitching and rolling moments were 11% and 9% smaller, respectively. Unlike the quadcopter equipped with variable-pitch rotors, the quadcopter equipped with variable-RPM rotors experienced a beating phenomenon in the aircraft-level vibratory loads.

NOTATION

Ω	Rotor rotational velocity
R	Rotor radius
x	Aircraft x-position (Inertial Frame)
y	Aircraft y-position (Inertial Frame)
z	Aircraft z-position (Inertial Frame)
ϕ	Aircraft roll attitude (Inertial Frame)
θ	Aircraft pitch attitude (Inertial Frame)
ψ	Aircraft yaw attitude (Inertial Frame)
u	Aircraft x-velocity (Body Frame)
v	Aircraft y-velocity (Body Frame)
w	Aircraft z-velocity (Body Frame)
p	Aircraft roll rate(Body Frame)
q	Aircraft pitch rate (Body Frame)
r	Aircraft yaw rate (Body Frame)
V_{hub}	Hub velocity
U_T	Tangential wind velocity
U_P	Perpendicular wind velocity
λ	Inflow Ratio $U_P/\Omega R$
μ	Advance Ratio $V/\Omega R$

Presented at the AHS Specialists' Conference on Aeromechanics Design for Transformative Vertical Flight, San Francisco, California, January 16-19, 2018 Copyright © 2018 by AHS International, Inc. All rights reserved.

INTRODUCTION

Multicopters are becoming increasingly popular in many areas including military, commercial, hobbyist, and law enforcement applications. Typically, multicopters make use of independent RPM control of each rotor in lieu of traditional collective and cyclic rotor pitch controls found on a conventional helicopter. This design allows for mechanical simplicity and relatively inexpensive production and maintenance. As the market for these aircraft has expanded, so too has the interest in different control methodologies and improvement in aircraft performance. Part of this interest has been in the design of multirotor aircraft that use collective pitch on feathering rotors instead of controlling the rotor speed. Such a design would be of particular interest as multicopers scale up in gross weight, where the rotor inertia would make variable-RPM control impractical.

A small number of studies have been conducted regarding the use of variable-pitch rotors on multicopter aircraft, including Gupta et al. (Ref. 1). In this study, a dynamic model of a variable-pitch quadrotor is presented using Blade Element Theory and Momentum theory to determine thrusts. A nonlinear controller is then designed using dynamic inversion, derived using the total 6 degree of freedom model. This control design is then demonstrated through simulation to track a desired trajectory.

Pang et al. (Ref. 2) explored the possibility of utilizing a gaso-

line engine on a variable-pitch quadrotor to improve flight endurance of the aircraft. Blade element theory with uniform inflow is used in the design of these rotors, with the assumption of linear aerodynamics for the operational regime of the rotor. The study produced an aircraft with an estimated 2.8 hour hover endurance at a 10 kg maximum take-off weight.

More recently, Abhishek et al. (Ref. 3) presented the design and development of a gasoline engine-driven, variable-pitch controlled quadrotor using Blade Element Momentum Theory to model the rotors at different rotational speeds and pitch angles, validating their model with experimental data. The authors demonstrated the ability to control such an aircraft and extend their analysis to a 10 kg platform, which they estimated to offer a hover endurance greater than 2 hours.

Cutler et al. (Refs. 4, 5) formulate a model similar to Pounds (Ref. 6) using an analysis code based in blade element momentum theory (Ref. 7), in order to account for the pitch setting on a variable-pitch rotor. Their model assumes linear aerodynamics, which will hold in a large portion of the operational regime of the rotor, but will break down in the nonlinear aerodynamic regime near stall. The study concludes that use of variable-pitch actuation enables faster aircraft response relative to the fixed-pitch aircraft, as well as the ability to choose between efficient and agile operation, and introduces the ability to reverse rotor thrust easily. Cutler and How (Ref. 8) go on to develop a controller and trajectory planner for variable-pitch quadrotors that allows for aerobatic maneuvers within control limitations. Cutler also details hardware implementation and flight testing for such aircraft in Ref. 9.

Recently, some studies have focused on the modeling and dynamic simulation of small multicopters. Typically, the model used assumes that the thrust and torque generated by the rotor is proportional to the square of the rotor speed (Ref. 6). This model is dependent on thrust test data and is restricted to hovering flight. Models based in Blade Element Momentum Theory are similarly restricted to axial flight conditions; moments that arise in forward flight are not captured whatsoever. Blade Element theory can capture these moments, but are dependent on the choice of inflow model. Uniform inflow will capture the drag and rolling moment, but Niemiec and Gandhi (Ref. 10) demonstrate that this model fails to capture rotor hub pitch moments, as well as the rotor side forces. The authors go on to demonstrate that a dynamic inflow coupled with Blade Element Theory is able to predict these hub forces and moments, indicating that the choice of rotor model influences the simulated aircraft performance in various flight conditions.

This higher-fidelity model has not yet been applied to the analysis of these rotors to explore the fundamental differences in the rotor performance between variable-pitch and variable-RPM control. The present work seeks to compare the two rotor control methods in terms of an isolated rotor performance, as well as potential impacts on aircraft performance in terms of aircraft power, dynamics, and vibratory loading.

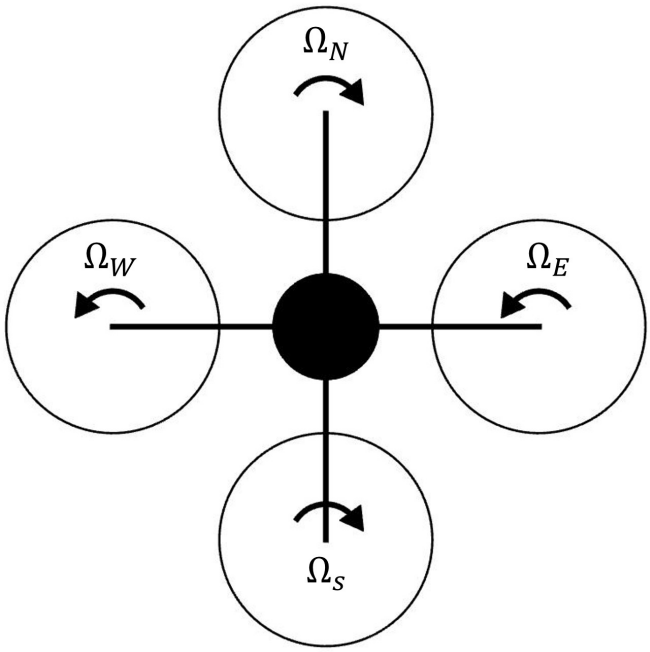

Fig. 1. Plus-type Quadcopter

MODELING

Aircraft Specifications

The present study is based on the AeroQuad Cyclone ARF Kit, a 2kg off-the-shelf quadcopter. The aircraft is flown with four rotors arranged in a plus (+) configuration (Fig. 1). The four APC 12x5.5 rotors are located 30.48cm from the geometric center of the aircraft. For the purposes of this study, the airfoil sections are assumed to be a NACA4412 at the root of the blade and a Clark Y outboard, with linear interpolation of aerodynamic properties in between. Twist and chord also vary linearly throughout the span. A summary of the rotor geometry can be found in Table 1.

Table 1. 12×5.5 APC Propeller Geometry

Parameter	Value
Rotor Radius	15.24 cm
Root Pitch	21.5°
Tip Pitch	11.1°
Root Chord	3.1 cm
Tip Chord	1.2 cm
Root Airfoil Section	NACA 4412
Tip Airfoil Section	Clark Y

Rotor Model

The rotor model assumes rigid blades and utilizes a Blade Element Theory model with a 3×4 (10 State) Peters-He finite state dynamic wake model (Ref. 11) to calculate rotor induced velocities. Sectional aerodynamic forces and moments are integrated along the span and about the azimuth to obtain rotor

hub forces (thrust, drag, and side force) and moments (torque, pitching, and rolling moments). The details of the rotor model are outlined in (Ref. 10), they are repeated here for convenience.

On any sectional blade element, the angle of attack is defined by three parameters; blade pitch (θ), tangential velocity (U_T), positive leading edge to trailing edge, and perpendicular velocity (U_P), positive downward. The tangential velocity (U_T) is comprised of two components; one from the rotational speed of the rotor (Ω times the distance from the center of rotation), the other from the free stream velocity.

U_P, the perpendicular velocity component, results from 3 contributors; the rotor induced velocity (λ_i), the vertical velocity of the hub, and the rotation about the aircraft hub. With this, the tangential and perpendicular velocities at a blade section are given by Eq. 1.

$$\begin{aligned} U_T &= \Omega r_b + V_{hub,x}\sin\psi_b + (-1)^k V_{hub,y}\cos\psi_b \\ U_P &= \Omega R\lambda_i + V_{hub,z} - (-1)^k r_b p\sin\psi_b - r_b q\cos\psi_b \end{aligned} \tag{1}$$

where r_b is the span-wise location of the blade section, ψ_b is the azimuthal position of the blade section, and k is a parameter that takes zero value for counterclockwise-spinning rotors and takes a value of 1 for clockwise-spinning rotors.

The inflow ratio (λ_i) for the rotor is defined using a 3×4 Peters-He (Ref. 11) finite state dynamic wake model. This model defines the induced inflow distribution by Eq. 2.

$$\lambda_i = \sum_{m=0}^{\infty}\left(\sum_{n=m+1,m+3,\ldots}^{\infty}\phi_n^m(\bar{r})\left[\alpha_n^m\cos(m\psi_b) + \beta_n^m\sin(m\psi_b)\right]\right) \tag{2}$$

where $\bar{r} = r_b/R$ is the normalized radial position.

The parameters α_n^m and β_n^m in the above equations can be determined by Eq. 3.

$$\begin{aligned} \Omega\{K_m^{nc}\}\{\dot{\alpha}_n^m\} + V[\bar{L}_s]^{-1}\{\alpha_n^m\} &= \frac{1}{2}\{\tau_n^{mc}\} \\ \Omega\{K_m^{nc}\}\{\dot{\beta}_n^m\} + V[\bar{L}_s]^{-1}\{\beta_n^m\} &= \frac{1}{2}\{\tau_n^{ms}\} \end{aligned} \tag{3}$$

Where:

$$\{\tau_n^{0c}\} = \frac{1}{2\pi}\sum_{q=1}^{N_b}\int_0^1 \frac{L}{\rho\Omega^2R^3}\phi_n^0(\bar{r})d\bar{r}$$

$$\{\tau_n^{mc}\} = \frac{1}{\pi}\sum_{q=1}^{N_b}\int_0^1 \frac{L}{\rho\Omega^2R^3}\phi_n^m(\bar{r})d\bar{r}\cos(m\psi_b)$$

$$\{\tau_n^{ms}\} = \frac{1}{\pi}\sum_{q=1}^{N_b}\int_0^1 \frac{L}{\rho\Omega^2R^3}\phi_n^m(\bar{r})d\bar{r}\sin(m\psi_b)$$

These equations are implicitly nonlinear in α_n^m and β_n^m, and are solved such that the average values of $\dot{\alpha}_n^m$ and $\dot{\beta}_n^m$ are equal to zero.

With U_P and U_T defined for a blade section, the inflow angle (ϕ_i) can be defined by Eq. 4, consequently the sectional angle of attack can be defined by Eq. 5. Note that in Eq. 5, θ is the geometric pitch of the blade section.

$$\phi_i = \tan^{-1}\frac{U_P}{U_T} \tag{4}$$

$$\alpha = \theta - \phi_i \tag{5}$$

Now, elemental lift and drag are defined by the angle of attack and incident velocities (Eq. 6)

$$\begin{aligned} dL &= \frac{1}{2}C_l(\alpha, r_b)\rho(U_T^2 + U_P^2)c\,dr_b \\ dD &= \frac{1}{2}C_d(\alpha, r_b)\rho(U_T^2 + U_P^2)c\,dr_b \end{aligned} \tag{6}$$

The lift and drag are then rotated by ϕ_i to resolve the forces into components normal and tangential to the rotor disk (Eq. 7).

$$\begin{aligned} dF_x &= -dL\sin\phi_i + dD\cos\phi_i \\ dF_z &= dL\cos\phi_i - dD\sin\phi_i \end{aligned} \tag{7}$$

The two terms in the expression for dF_x represent the induced drag and the profile drag, respectively. Their respective contributions to the rotor power are referred to as the induced power and profile power. These blade elemental forces contribute to the rotor drag (H-force, positive forward), side force (Y-force, positive right), and thrust (T, positive downward). These contributions are detailed in Eq. 8. Rotor moments are also impacted by the elemental forces (Eq. 9). These include the rolling moment (M_x, positive roll-right), pitching moment (M_y, positive nose-up), and rotor torque (M_z, positive nose-right).

$$\begin{aligned} dH &= -dF_x\sin\psi_b \\ dY &= -(-1)^k dF_x\cos\psi_b \\ dT &= -dF_z \end{aligned} \tag{8}$$

$$\begin{aligned} dM_x &= -(-1)^k dF_z r_b\sin\psi_b \\ dM_y &= -dF_z r_b\cos\psi_b \\ dM_z &= (-1)^k dF_x r_b \end{aligned} \tag{9}$$

The average rotor forces and moments are found by integrating the elemental contributions along the blade span and about the azimuth, then summed over the number of blades and averaged over one revolution. As such, the expression for rotor thrust is given by Eq. 10.

$$T = \frac{N_b}{2\pi}\int_0^{2\pi}\int_0^R dT \; dr_b \, d\psi_b \tag{10}$$

Other total rotor forces can be found with similar expressions, substituting the appropriate elemental contributions from Eqs. 8 and 9.

Aircraft Trim and Autonomous Dynamics

The 6 rigid body equations of motion are given in Eq. 11. These equations reflect a summation of forces and moment about the center of gravity of the aircraft (assumed to lie beneath the rotor plane at the geometric center of the aircraft). Gyroscopic moments are neglected due to the small net angular momentum of the rotors (equal number of clockwise and counterclockwise-spinning rotors).

$$\begin{aligned}
m\dot{u} &= D_{fuse,x} - g\sin\theta + \sum_{i=1}^{4} H_i \\
m\dot{v} &= D_{fuse,y} - g\sin\phi\cos\theta + \sum_{i=1}^{4} Y_i \\
m\dot{w} &= D_{fuse,z} + g\cos\phi\cos\theta + \sum_{i=1}^{4} T_i \\
I_{xx}\dot{p} &= -z_{cg}mg\sin\phi\cos\theta + \sum_{i=1}^{4}(M_{x_i} + T_i y_i) \\
I_{yy}\dot{q} &= -z_{cg}mg\sin\theta + \sum i = 1^4 (M_{y_i} + T_i x_i) \\
I_{zz}\dot{r} &= \sum_{i=1}^{4}(M_{z_i} + Y_i x_i - H_i y_i)
\end{aligned} \tag{11}$$

Setting the accelerations to zero yields an algebraic system of equations, which are solved using a Newton-Rhapson method for the rotor speeds (or root pitch setting) in multi-rotor coordinates (Ref. 12). From the trim solution, key quantities such as aircraft and rotor power can be extracted for further analysis. The power of an individual rotor can be determined by Eq. 12, total aircraft power can then be found by the sum of these individual rotor powers.

$$\begin{aligned}
P_i &= \tau_i \Omega_i = M_{z_i}\Omega_i \\
P_{tot} &= \sum_{i=1}^{4} P_i
\end{aligned} \tag{12}$$

Aircraft bare airframe dynamics are also considered in the present study. For this, the nonlinear system (Eqs. 3, 11) is numerically linearized about a trim point using centered finite differences to generate a linear model of the form given in Eq. 13.

$$\begin{aligned}
\dot{x} &= f(x,u) \\
y &= g(x,u)
\end{aligned} \quad \longmapsto \quad \begin{aligned}
\dot{x} &= Ax + Bu \\
y &= Cx + Du
\end{aligned} \tag{13}$$

where:

$$A \in \mathbb{R}^{n\times n} \qquad B \in \mathbb{R}^{n\times m}$$
$$C \in \mathbb{R}^{n_o\times n} \qquad D \in \mathbb{R}^{n_o\times m}$$

Here, n is the number of states, m is the number of inputs, and n_o is the number of outputs.

In order to approximate the nonlinear system, the matrices A and B take the form of Eq. 14 (for the present study $n_o = 0$, therefore C and D are empty).

$$\begin{aligned}
A &= \begin{bmatrix} \frac{\partial \dot{x}_1}{\partial x_1} & \frac{\partial \dot{x}_1}{\partial x_2} & \cdots & \frac{\partial \dot{x}_1}{\partial x_n} \\ \frac{\partial \dot{x}_2}{\partial x_1} & \frac{\partial \dot{x}_2}{\partial x_2} & \cdots & \frac{\partial \dot{x}_2}{\partial x_n} \\ \vdots & \vdots & \ddots & \vdots \\ \frac{\partial \dot{x}_n}{\partial x_1} & \frac{\partial \dot{x}_n}{\partial x_2} & \cdots & \frac{\partial \dot{x}_n}{\partial x_n} \end{bmatrix} \\
B &= \begin{bmatrix} \frac{\partial \dot{x}_1}{\partial u_1} & \frac{\partial \dot{x}_1}{\partial u_2} & \cdots & \frac{\partial \dot{x}_1}{\partial u_m} \\ \frac{\partial \dot{x}_2}{\partial u_1} & \frac{\partial \dot{x}_2}{\partial u_2} & \cdots & \frac{\partial \dot{x}_2}{\partial u_m} \\ \vdots & \vdots & \ddots & \vdots \\ \frac{\partial \dot{x}_n}{\partial u_1} & \frac{\partial \dot{x}_n}{\partial u_2} & \cdots & \frac{\partial \dot{x}_n}{\partial u_m} \end{bmatrix}
\end{aligned} \tag{14}$$

Because the Peters-He model is used to calculate inflow, there are a number of states (4 rotors $\times$ 10 states per rotor) associated with the inflow dynamics. The poles associated with the inflow are very far in the left half-plane, and the technique of static condensation is applied to reduce the size of the system. If x, A, and B are partitioned as in Eq. 15, then the linear model Eq. 13 becomes the system defined by Eq. 16

$$x = \begin{bmatrix} x_b \\ x_i \end{bmatrix} \qquad A = \begin{bmatrix} A_{bb} & A_{bi} \\ A_{ib} & A_{ii} \end{bmatrix} \qquad B = \begin{bmatrix} B_b \\ B_i \end{bmatrix} \tag{15}$$

$$\begin{aligned}
\dot{x_b} &= A_{bb}x_b + A_{bi}x_i + B_b u \\
\dot{x_i} &= A_{ib}x_b + A_{ii}x_i + B_i u
\end{aligned} \tag{16}$$

Setting $\dot{x_i} = 0$ (treating it as static) and solving for x_i yields:

$$x_i = -A_{ii}^{-1}(A_{ib}x_b + B_i u) \tag{17}$$

Substitution into Eq. 16 yields the condensed model Eq. 18

$$\begin{aligned}
\dot{x_b} &= (A_{bb} - A_{bi}A_{ii}^{-1}A_{ib})x_b + (B_b - A_{ii}^{-1}B_i)u \\
&= \bar{A}x_b + \bar{B}u
\end{aligned} \tag{18}$$

Vibrations Analysis

To assess the vibratory loading on an isolated rotor, Eq. 3 is solved in a steady sense for a fixed Ω and incident velocity (obtained from the trim analysis), and the blade root shears are evaluated by integrating Eq. 7 along the radius of the blade. Root bending moments are evaluated similarly, with

appropriate consideration of the moment arm. These shears and moments (defined with respect to the rotating blade) are rotated into the hub frame (which is non-rotating) via Eqs 8, 9, and summed across the two blades, phased by 180°.

When considering the loading at the aircraft level, the vibratory forces are simply superimposed on one another, and moments from rotor hub loads and induced moments are similarly superimposed. Unless specifically noted otherwise, forces and moments that act at the same frequency are assumed to be in-phase, representing a worst-case scenario for vibratory loading.

ISOLATED ROTOR RESULTS

Static Thrust Performance

Static thrust simulations were performed to compare the performance of a variable-RPM rotor with different root pitch settings, using the geometric parameters in Table 1. The range of rotor speeds considered in this study is 2000-8000RPM.

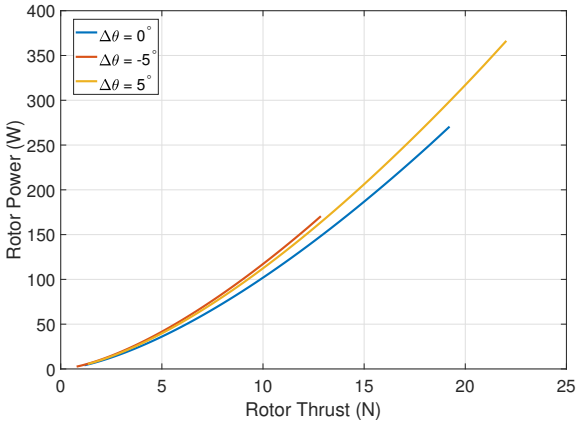

Fig. 2. Variable-RPM Rotor Power Requirement vs Thrust Output

Figure 2 shows the relationship between thrust and power for the Aeroquad Cyclone rotor, where $\Delta\theta$ is the change in root pitch setting from the value given in Table 1 (21.5°). The required power for any given thrust appears to be lowest for a $\Delta\theta$ of 0°, suggesting that the rotor is well-designed for hover. The thrust and power coefficients for these rotors can also be compared for the same range of RPM simulated in Fig. 2, these values are given in Fig. 3.

The concept of thrust and power coefficients for a variable-RPM rotor is unique in the discussion of rotary wing vehicles. Because these rotors generate different thrust (and consequently consume more power) by changing the rotational speed of the rotor, the denominator in the expression for both coefficients (Eq. 19) changes for different values of thrust and power.

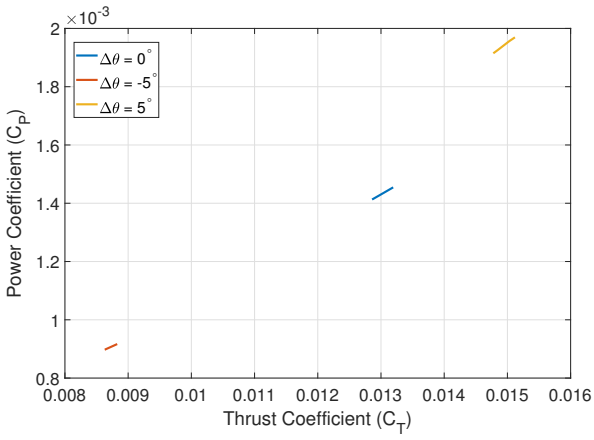

Fig. 3. Variable-RPM Rotor C_P vs C_T

$$C_T = \frac{T}{\rho\pi R^2 v_{tip}^2} = \frac{T}{\rho\pi R^4\Omega^2}$$
$$C_P = \frac{P}{\rho\pi R^2 v_{tip}^3} = \frac{\tau\Omega}{\rho\pi R^5\Omega^3} \quad (19)$$

From these expressions, if T and τ increase with Ω^2, an intuitive result that is the basis of much multicopter modeling (Refs. 4, 6), then the thrust and power coefficients would remain constant over the entire operating regime of the rotor. Therefore, unlike in variable-pitch systems, C_T and C_P are *not direct proxies for rotor thrust and power*. If analysis is restricted to hover, then C_T and C_P are proportional to the coefficients used in the Ω^2 model. Due to slight deviations from this result due to compressibility corrections, the values of C_P and C_T vary slightly with rotor thrust in Fig. 3.

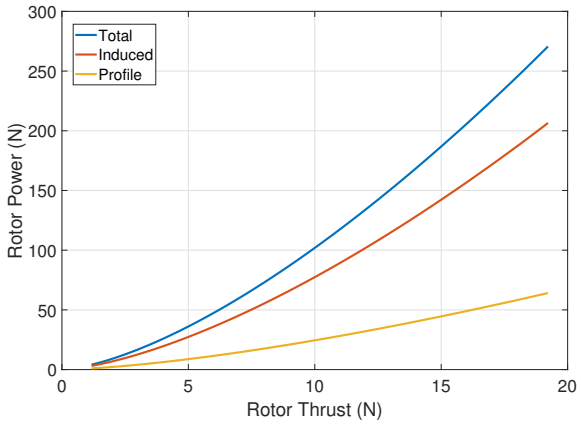

Fig. 4. Power Contributions vs Thrust Output for the variable-RPM Rotor

The rotor power can be broken down into induced power and profile power, as in Fig. 4. As expected from momentum theory, the induced power increases with the $T^{3/2}$. Additionally, the profile power increases with $T^{3/2}$. Lift and drag share this

structure because the changes in lift and drag come not from a change in lift and drag coefficients, but from the change in dynamic pressure. Consequently, the share of power from induced drag (76%) and profile drag (24%) remains constant with respect to rotor thrust. This breakdown is specific to this rotor geometry; any changes to the twist, solidity, or airfoil distribution will change this ratio.

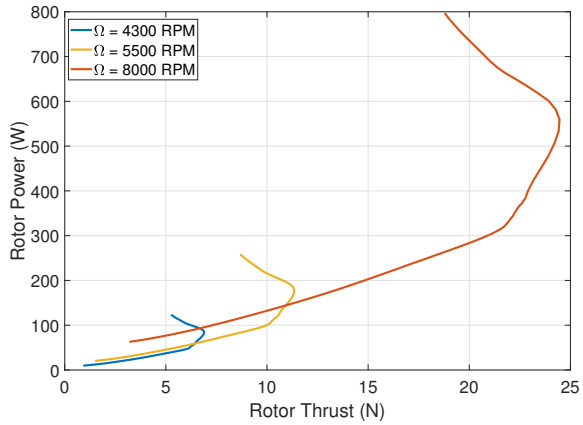

Fig. 5. Variable-Pitch Rotor Power Requirement vs Thrust Output

A similar study was conducted varying the root pitch setting of the rotor for discrete values of Ω. Figure 5 is the required power for the generation of thrust for $\Delta\theta$ ranging from -12° to 12° difference from the nominal root pitch of the rotor (21.5°), or a variation in root pitch from $9.5^\circ$to 33.5°, for nominal rotational speeds of 4300, 5500, and 8000 RPM. These speeds correspond to the speed at which the nominal variable-RPM rotor produces 0.5 kg of thrust (4300 RPM), which is the hover trim thrust for the quadcopter being considered, the maximum operational speed of the rotor (8000 RPM), and a nominal rotor speed (5500 RPM), the significance of which will be discussed later in the present section.

With the rotor operating at a constant rotational speed, a change in geometric pitch corresponds to a change in the sectional angle of attack seen along the span of the rotor. As such, there is a distinct region in Fig. 5 that depicts where the blade is operating in the linear aerodynamic regime, indicated by the smooth section of the power curve at lower values of rotor thrust, followed by a sharp increase in the rotor power when the blade approaches stall.

Typically, a small-scale multicopter is designed to allow for a 2:1 maximum thrust-to-weight ratio. For the AeroQuad Cyclone, this corresponds to each rotor being able to carry approximately 10N of thrust at maximum output. While the variable-RPM rotor is certainly capable of this level of thrust (Fig. 2), the variable-pitch design at a nominal speed of 4300 RPM (Fig. 5, blue) has a maximum thrust output significantly less than the 10 N requirement. Operation at 8000RPM (Fig. 5, red) increases the margin well beyond 2:1, at the cost of power at normal loads (105% over the rotor at 4300RPM at 5N thrust). At 5500 RPM (Fig. 5, yellow), the variable-pitch rotor is able to attain a maximum thrust of 10N prior to rotor stall, while consuming 23% more power than the 4300 RPM rotor at 5N thrust. As such, this rotor will be considered as the nominal variable-pitch rotor henceforth.

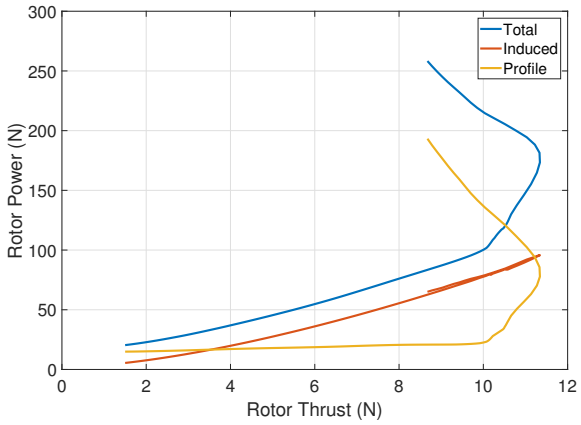

Fig. 6. Power Contributions vs Thrust Output for the Nominal Variable-Pitch Rotor (5500 RPM)

The power required by the nominal variable-pitch rotor is broken down into its induced and profile components in Fig. 6. The induced power, as expected from momentum theory, follows $T^{3/2}$, as the variable-RPM rotor did. However, the profile drag does not follow the same pattern. This is because of the dependence on changes in the drag on the drag coefficient of the blade. Over the linear aerodynamic regime (<10N thrust), the profile power is insensitive to the thrust generated, as the drag coefficient is insensitive to the angle of attack in this regime. However, as the blade approaches stall, the drag coefficient diverges, with little change in the lift coefficient, resulting in the dramatic increase in power.

Because the variable-pitch rotor operates at a constant rotational speed, the conventional understanding of rotor thrust and power coefficient as an analogue to rotor thrust and power applies. These coefficients are displayed in Fig. 7 for the different rotational speeds considered. The curves are coincident, with slight difference at larger C_T values because of the applied compressibility corrections.

The thrust and power of the chosen nominal variable-RPM and variable-pitch rotors are plotted in Fig. 8. As expected, the two curves intersect at the point where the variable-pitch rotor is at $\theta_0 = 21.5^\circ$ ($\Delta\theta = 0$) and the variable-RPM rotor is operating at 5500 RPM, as both rotors are operating at identical settings. For the majority of the thrust outputs, the variable-RPM rotor consumes less power than the variable-pitch rotor. This is due to the larger profile power of the variable-pitch rotor (Fig. 6) from its operating at a higher speed (required for stall margin) in the region prior to the intersection of the curves. In all operating conditions, the induced power of both rotors is identical. At 5N, the variable-pitch rotor requires 29% more power than the variable-RPM

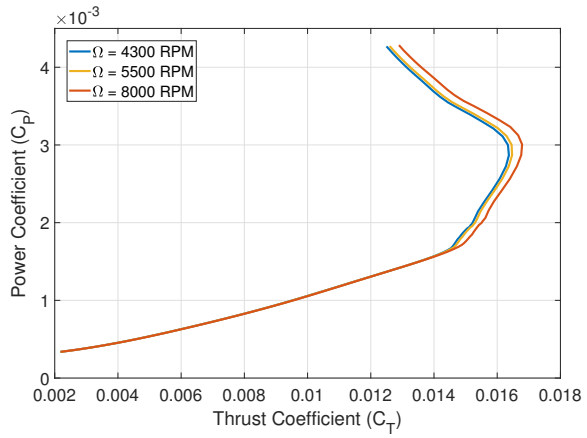

Fig. 7. Variable-Pitch Rotor C_P vs C_T

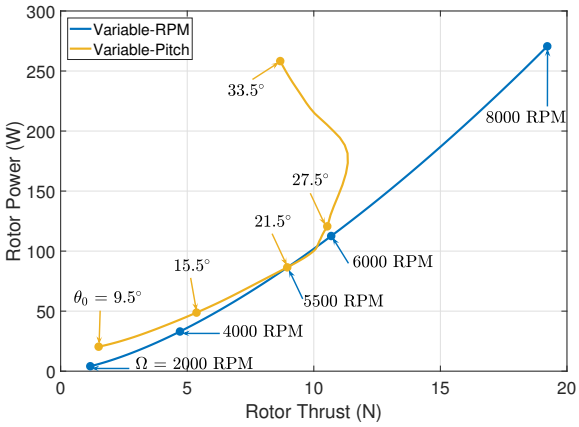

Fig. 8. Nominal Rotor Comparison, Power Requirement vs Thrust Output

rotor due to the higher operating speed needed for thrust margin.

Climb Performance

To simulate axial climb, $V_{hub,z}$ was set between 0 (hover) and 20 m/s, and Ω (variable-RPM) or θ_0 (variable-pitch) was solved such that the rotor generated 5N thrust. The power requirement for each rotor versus the climb rate is presented in Fig. 9.

As the climb velocity increases, the rotor experiences increasing downwash, manifesting as an increase in U_P in Eq. 4. Absent compensation, the increase in ϕ tends to decrease the angle of attack α (Eq. 5) and cause a subsequent loss of lift. The variable-pitch rotor compensates by simply increasing θ, while the variable-RPM rotor can only increase Ω. Increasing Ω increases thrust by reducing the magnitude of ϕ (by increasing U_T) and increasing the dynamic pressure. The maximum climb rate reached by the variable-RPM rotor is 15.25 m/s; at this speed, the angles of attack are too low for even the (relatively) high tip speed to compensate; additionally, the

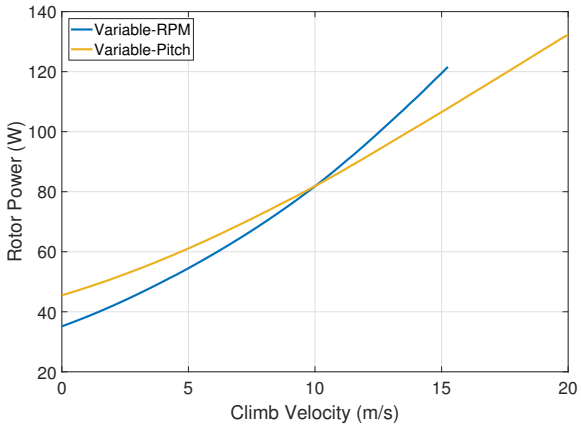

Fig. 9. Power Requirements vs Climb Velocity

rotor is spinning at its maximum speed and has no remaining margin. The variable-pitch rotor does not reach a limit until 21.75 m/s (43% greater than the variable-RPM rotor), where the root pitch setting is 33.5°, an arbitrarily imposed maximum. If larger pitch angles are allowed, the limit on motor power (200W) is reached at 26 m/s (70% greater than the variable-RPM rotor). Overall, the variable-RPM rotor is more efficient in hover and at low rates of climb; it also has a lower maximum rate of climb and has higher power requirements than the variable-pitch rotor near its maximum rate of climb.

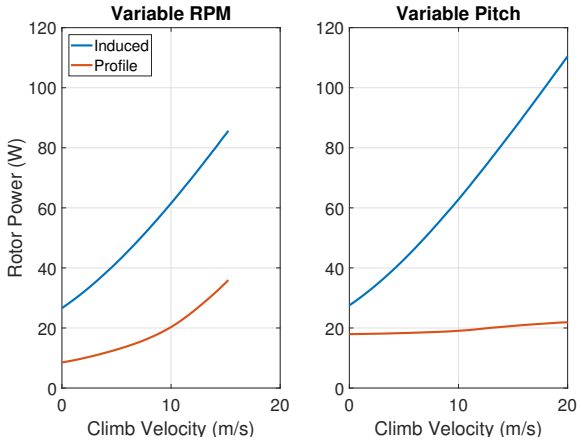

Fig. 10. Power Contributions vs Climb Velocity for Different Rotor Types

The power requirements for both the variable-RPM and variable-pitch rotors are broken down into induced and profile power in Fig. 10. Both rotors experience a nearly identical change in induced power, consistent with expectations from momentum theory. However, the profile power of the variable-RPM rotor is much more sensitive to climb rate than that of the variable-pitch rotor. This is due to the adverse effect of increasing the dynamic pressure to compensate for reduced lift in climb. Because the variable-pitch rotor changes θ to compensate for climb, α is changed little, and the drag

coefficient is similarly insensitive to climb. Consequently, the profile power is significantly less sensitive to climb for the variable-pitch rotor.

FULL AIRCRAFT RESULTS

Trim

Two quadcopter configurations are considered for analysis in trimmed flight between hover and 15 m/s, one with variable-RPM rotors and the other with variable-pitch rotors. Trim controls for the variable-RPM aircraft are given in Fig. 11. Hover trim requires the four rotors to operate at the same rotational speed in order to generate only thrust. As the aircraft transitions into forward flight, rotor hub drag and pitching moments become significant along with a net drag force and pitching moments coming from the aircraft hub. This is compensated by differential RPM between the north (front) rotor and south (rear) rotor to compensate for the nose-up pitching moment, as well as the aircraft pitching nose-down to compensate for the net drag force. The variable-pitch rotor trim controls (Fig. 12) exhibits similar properties, with root pitch replacing rotor speed.

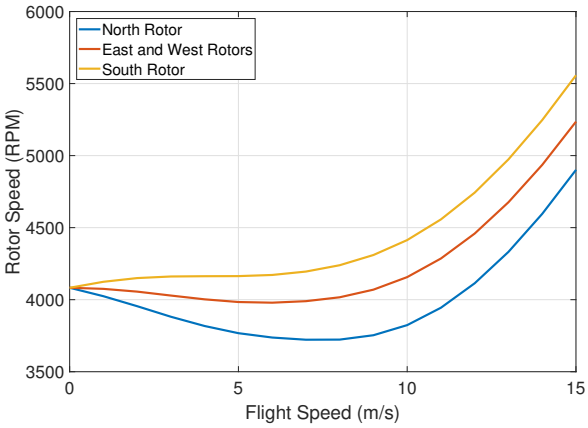

Fig. 11. Variable-RPM Trim Controls vs Flight Speed

The aircraft required power is plotted versus airspeed in Fig. 13. Both aircraft experience similar trends in power as the flight speed increases. Transitioning from hover to forward flight, the required power decreases. This reduction in power requirement is a result of the additional mass flux through the rotor reducing the velocity induced by the rotor. At higher speeds, the additional thrust required by increasing fuselage drag drives the overall power upward. In this regime, the variable-RPM rotor power grows more rapidly with flight speed than the variable-pitch rotor, though through 15 m/s it requires less power overall.

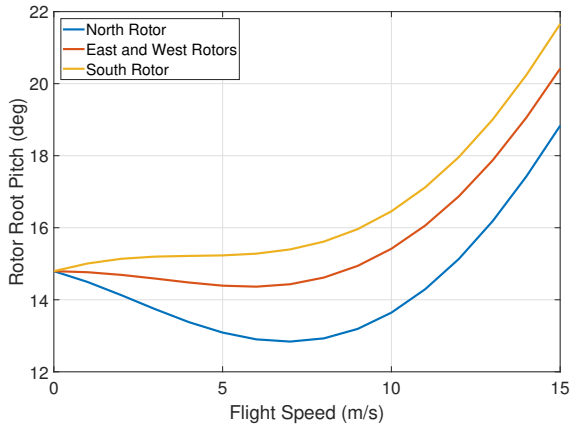

Fig. 12. Variable-Pitch Trim Controls vs Flight Speed

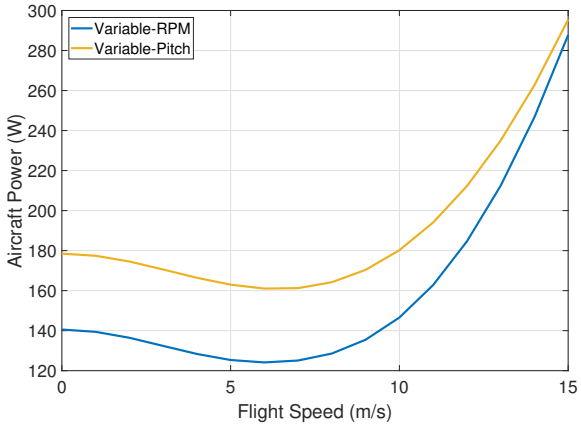

Fig. 13. Comparison of Trimmed Aircraft Power

The maximum endurance speed for the variable-RPM and variable-pitch rotors are 6 m/s and 6.5 m/s, respectively. At these speeds, the variable-pitch rotor requires 30% more power than the variable-RPM rotor. The speeds for maximum range, V_{br}, of the aircraft are defined by the point at which a line extending from the origin is tangent to the power curve. V_{br} for the aircraft with variable-RPM rotors is 10 m/s and is 11 m/s for the variable-pitch rotor aircraft. The required power at V_{br} is 32% higher for the variable-pitch aircraft, compared to the variable-RPM aircraft. This corresponds to a 18% reduction in range.

Bare Airframe Dynamics

The bare aircraft dynamics of the aircraft system can be described by performing an eigenanalysis of the reduced-order linearized system given in Eq. 18. The characteristics of the dynamic modes can be examined by the location of the eigenvalues on the complex plane, which are plotted for both aircraft in Fig. 14 in the hover condition.

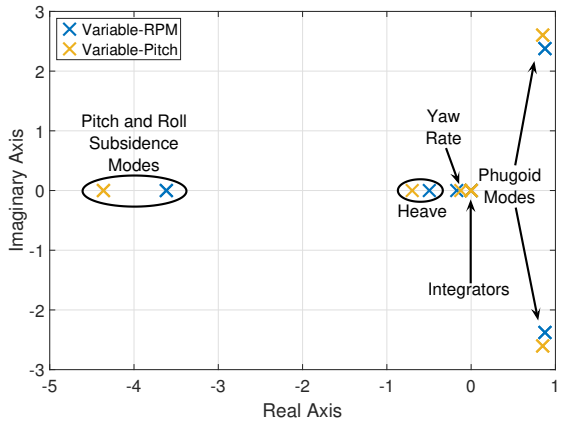

Fig. 14. Open-Loop Pole Locations for Both Aircraft in Hover

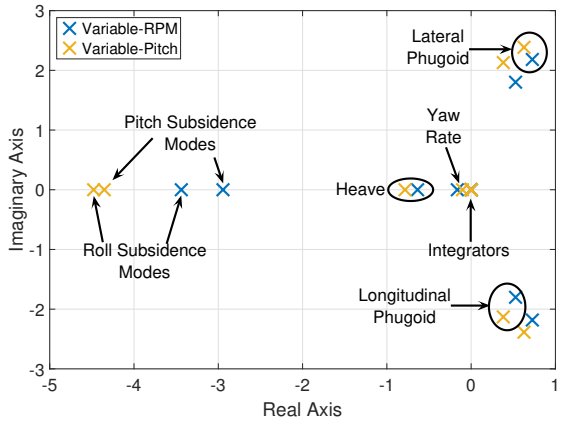

Fig. 15. Open-Loop Pole Locations for Both Aircraft in 5 m/s Forward Flight

There are twelve poles for each aircraft, corresponding to the twelve dynamic states in the reduced-order linear model. Farthest in the left half-plane are two subsidence modes associated with the roll and pitch of the aircraft, closer to the origin is the heave mode, and closer still to the origin is the yaw rate mode. At the origin, there are 4 integrators corresponding to the aircraft position and heading. Finally, there are two pairs of conjugate poles in the right half-plane that describe the phugoid modes for the aircraft (unstable oscillatory modes that couple roll and lateral translation for the lateral mode, and pitch and longitudinal translation in the longitudinal mode).

Comparing the pole locations for the two configurations, the largest difference is in the decay rate of the subsidence modes, with the variable-pitch aircraft having greater damping in these modes than the variable-RPM aircraft. The larger damping comes from the sensitivity of rotor thrust to heave motion, which is greater for the variable-pitch rotor than the variable-RPM rotor. Because of the lower angles of attack on the variable-pitch rotor, a change in U_P causes a greater percentage change in the angle of attack than on the variable-RPM rotor, resulting in a larger change in net thrust. This phenomenon drives the larger heave damping, which is the dominant factor in the subsidence and heave modes. This is also the primary driver of the differences between the locations of the phugoid mode poles, though it manifests as a change in the frequency. The integrators are naturally unaffected.

The poles of the two aircraft at 5m/s forward speed are plotted in Fig. 15. In forward flight, the poles corresponding to the longitudinal modes of the aircraft move closer to the origin while the poles corresponding to the lateral modes stay approximately in the same location as in Fig. 14. This causes the separation of the poles in the subsidence modes as well as the phugoid modes. However, the subsidence and heave modes for the variable-pitch aircraft still exhibit a larger decay rate than that of the variable-RPM aircraft, while the phugoid modes have higher natural frequency.

VIBRATORY LOADING

Isolated Rotor

Because the rotor is two-bladed, dominant hub loads will be transmitted to the fuselage at 2/rev. The magnitudes of the 2/rev vibrations are illustrated in Fig. 16. The 2/rev drag and side force have similar magnitudes to one another, and are 37% and 50% larger, respectively, for the variable-RPM rotor, compared to the variable-pitch rotor. The 2/rev thrust is substantially larger than the in-plane vibratory forces (12-13% of the mean rotor thrust), and is 6.5% smaller for the variable-RPM rotor. The hub pitching and rolling moments are smaller for the variable-RPM rotor (by 11% and 9%, respectively).

The in-plane forces are dominated by the blade root drag shear, and are given in the North-East-Down coordinate system by equation 20. The 2/rev components of these loads are given by equation 21, where S_{x_n} and ϕ_{x_n} are the magnitude of the n/rev component of the root drag shear the phase as given in Table 2, respectively. The hub pitch (M) and roll (L) moments are related to M_β in exactly the same way as H and Y respectively are to S_x. Because the rotation occurs about the hub z-axis, the 2/rev thrust is simply the 2/rev component of S_z multiplied by the number of blades. The dominant contributor to the periodic root loads is the azimuthal variation in dynamic pressure, and without cyclic pitch, this manifests as a strong 1/rev signal in each of the root loads. Other harmonics are derived primarily from the inflow distribution on the rotors and their effects on the aerodynamic loading on the blades. The components of these root loads are tabulated in Table 2.

$$H = -S_x \sin\psi \qquad Y = -S_x \cos\psi \tag{20}$$

$$\begin{aligned} H_2 &= \sqrt{S_{x_1}^2 + S_{x_3}^2 - 2S_{x_1}S_{x_3}\cos(\phi_{x_1} - \phi_{x_3})} \\ Y_2 &= \sqrt{S_{x_1}^2 + S_{x_3}^2 + 2S_{x_1}S_{x_3}\cos(\phi_{x_1} - \phi_{x_3})} \end{aligned} \tag{21}$$

Table 2. Fourier Coefficients of blade root loads

Fourier Coefficient		S_x		S_z		M_β	
		VR	VP	VR	VP	VR	VP
Steady	Magnitude	0.4283	0.3998	2.5000	2.5000	0.2594	0.2547
1/rev	Magnitude	0.2205	0.1548	1.1724	1.2080	0.1209	0.1347
	Phase	86°	101°	121°	142°	129°	150°
2/rev	Magnitude	0.0236	0.0253	0.3050	0.3258	0.0368	0.0385
	Phase	181°	221°	273°	273°	278°	277°
3/rev	Magnitude	0.0058	0.0109	0.1140	0.1171	0.0135	0.0139
	Phase	289°	306°	343°	341°	344°	342°

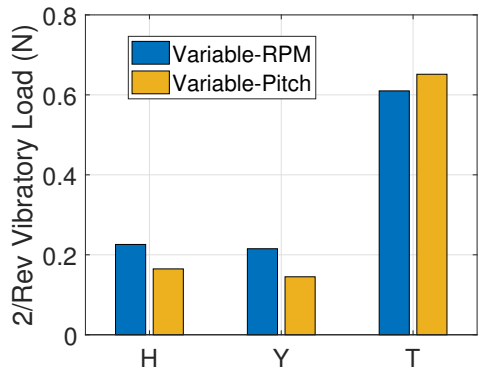

(a) Hub Forces

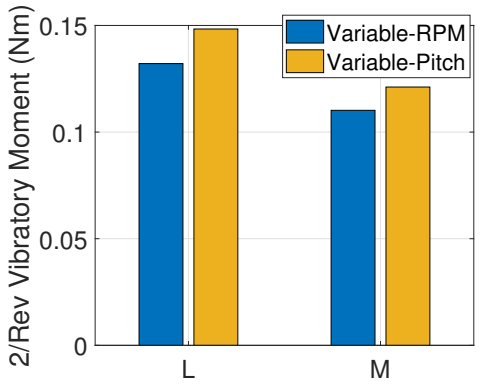

(b) Hub Moments

Fig. 16. 2/Rev hub Loads on rotor generating 5N thrust at 10 m/s

The root drag shear of a rotor producing 5N of thrust in a 10 m/s flow with a 15°nose-down attitude (representative of the trim condition) are shown in Fig. 17. The 1/rev root drag shear, the dominant contributor to the 2/rev H-force and Y-force, is 42% greater on the variable-RPM rotor than the variable-pitch rotor. The drag shear can be decomposed into two components, one from induced drag and another from profile drag, which are also plotted in Fig. 17. The 1/rev induced drag is 67% greater on the variable-RPM rotor than the variable-pitch rotor. The induced and profile drag are both dominated by the 1/rev dynamic pressure oscillation, which is maximum at $\psi = 90°$, and the induced component of drag is much greater than the profile drag.

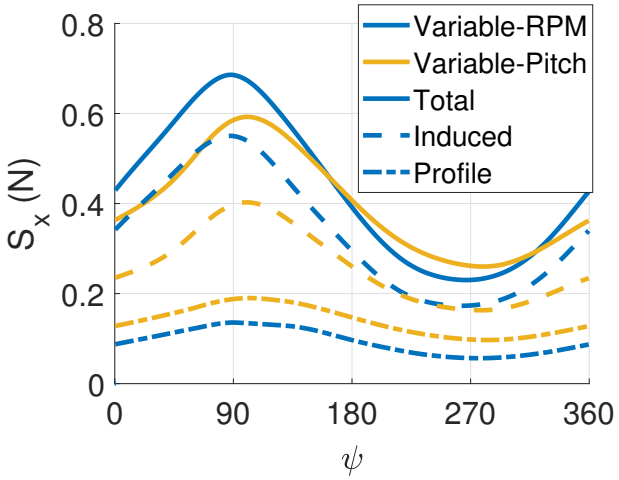

Fig. 17. Decomposed drag shear for 5N Thrust generation at 10 m/s, 15°nose-down

An explanation for the difference in the induced drag can be obtained from blade element theory. The lift generated by a blade element is given by Eq. 6. The dominant steady and 1/rev component of the elemental lift is given by Eqs. 22 and 23. Because the rotors generate the same amount of steady thrust, and Ω is greater for the variable-pitch rotor, the magnitude of $C_{L_{\text{steady}}}$ must be smaller. Roughly speaking, $C_{L_{\text{steady}}}$ should be approximately proportional to Ω^{-2}. The values of C_L at 75% blade span for both rotors is plotted in Fig. 18, and the steady value of C_L for the variable-pitch rotor is indeed smaller than that of the variable-RPM rotor (for stall margin). Considering this in the context of Eq. 23, the magnitude of the 1s component of the lift should be proportional to Ω^{-1}. Because Ω on the variable-pitch rotor is greater than that of the variable-RPM rotor, the 1/rev lift (and thus, the induced drag) is smaller.

$$dL_0 = \frac{1}{2} c C_{L_{\text{steady}}} \rho \Omega^2 r_b^2 dr_b \tag{22}$$

$$dL_{1s} = c C_{L_{\text{steady}}} \rho \Omega r_b V_\infty \sin\psi dr_b \tag{23}$$

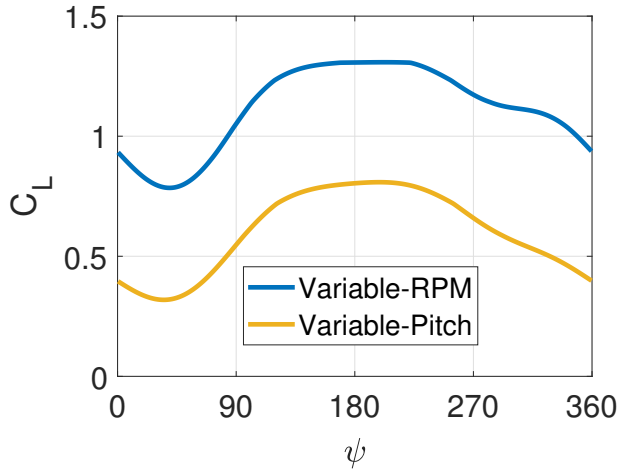

Fig. 18. Blade lift coefficient for rotors generating 5N thrust at 10 m/s, 75% span

Full Aircraft

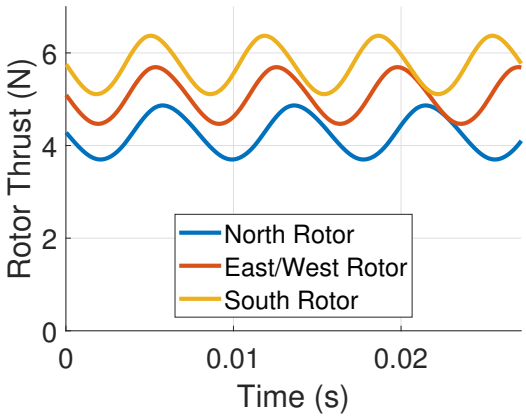

(a) Variable-RPM Rotor

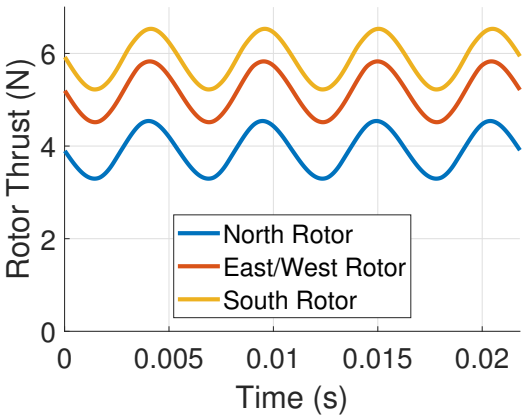

(b) Variable-Pitch Rotor

Fig. 19. Hub thrust for quadcopter trimmed at 10 m/s forward flight

The individual rotor hub loads can be summed to predict the aircraft-level steady and vibratory loads. For a trimmed quadcopter at 10 m/s forward flight, the individual rotor vertical loads are presented in Fig. 19. The variable-RPM rotors (Fig. 19(a)) all operate at different speeds, and thus the aircraft level vibrations occur at multiple nearby frequencies, while the variable-pitch rotors (Fig. 19(b)) all spin at the same speed and produce vibrations at identical frequencies. The differences in rotor speeds in the variable-RPM case produces a beating phenomenon at the aircraft level (Fig. 20), as the rotors move in and out of phase with one another. This does not occur on the variable-pitch rotor, as the rotors are effectively phase-locked by the operational speed. Overall, the magnitude of the vertical vibrations of the variable-pitch aircraft (assuming all rotor's thrusts are perfectly in phase) is equal to the maximum amplitude of the vertical vibrations of the variable-RPM rotor, although in theory, the variable-pitch rotors could be phased to reduce this vibration.

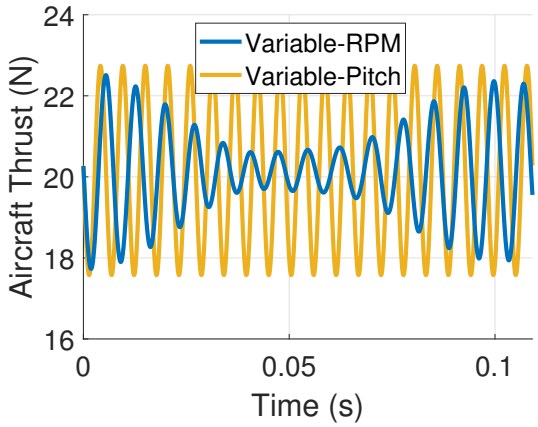

Fig. 20. Total Aircraft Thrust for a quadcopter trimmed at 10 m/s

CONCLUSIONS

For a quadcopter with a nominal gross weight of 20N, the current study examines the use of variable-pitch rotors compared to variable-RPM rotors across a variety of performance metrics. In hover, the variable-RPM rotor (based on the AeroQuad Cyclone quadcopter) was found to have a power-optimal root pitch, and the thrust and power coefficients were found not to change with rotor thrust. Thus, unlike pitch-controlled rotors, C_T and C_P are not proxies for the rotor thrust and power. The ratio of induced power to the total power was found to be 76% for the variable-RPM rotor, regardless of the thrust generated. In order to maintain a 2:1 maximum thrust-to-weight ratio, the variable-pitch rotor's rotational speed was increased to 5500RPM (from the nominal 4300 RPM for the variable-RPM rotor). Unlike the variable-RPM rotor, the ratio of induced to total power varied with the thrust generated, with the profile power increasing significantly at high thrust values approaching stall. At the nominal operating condition, generating 5N of thrust, the variable-pitch rotor requires 29%

more power than the variable-RPM rotor, as it operates at a higher RPM to preserve stall margin.

As the rotors climb, the downwash causes an increase in the induced inflow angle. The variable-RPM rotor compensates by increasing its speed, while the variable-pitch rotor increases its root pitch setting to maintain thrust. The maximum climb rate of the variable-RPM rotor was 15.25 m/s, at which point it was spinning at its maximum speed. The variable-pitch rotor has a greater maximum climb rate of 21.75 m/s (43% greater, corresponding to an arbitrarily assigned maximum root pitch setting of 33.5°), or 26 m/s (70% greater, at the maximum motor power). At low to moderate rates of climb, the variable-RPM rotor is more efficient, but near its maximum, the variable-RPM rotor requires more power than the variable-pitch rotor, due to the increase in profile power as the rotor tip speed increases.

Quadcopters equipped with variable-RPM and variable-pitch rotors were trimmed from hover to 15 m/s forward speed. To maintain a nose-down attitude to overcome aircraft drag, the rear (south) rotor needs to generate more thrust than the front (north) rotor, so the south rotor either spins faster or has a higher root pitch setting than the east and west rotors, and the north rotor spins slowest or has the lowest root pitch setting. Due to reduced induced velocity, all the rotors slow down or have lower pitch setting at moderate cruise speeds, while at high speeds, the additional thrust required to overcome drag causes the speed or pitch to grow rapidly. At all speeds considered, the variable-pitch aircraft required more power than the variable-RPM aircraft. At best-endurance speed, the variable-pitch aircraft requires 30% more power. At best-range speed, the variable-pitch aircraft has 18% less range.

Overall, the variable-pitch aircraft has larger heave damping on its rotors. This manifests as additional damping in the pitch and roll subsidence modes, as well as the heave mode. The phugoid modes have a higher natural frequency on the variable-pitch aircraft than the variable-RPM aircraft. In forward flight, the poles associated with the longitudinal modes move closer to the origin, while the lateral mode poles are unaffected. The longitudinal poles of the variable-pitch aircraft are farther from the origin than those of the variable-RPM aircraft.

At 10m/s cruise, the 1/rev root drag shear was 42% greater on the variable-RPM rotor than the variable-pitch rotor. This is driven primarily by the 1/rev induced drag, which is 67% greater on the variable-RPM rotor than the variable-pitch rotor. The 1/rev induced drag is reduced on the variable-pitch rotor because of the higher rotational velocity, which corresponds to a lower steady lift coefficient, and lower 1/rev induced drag shear.

At the rotor level, the 2/rev H- and Y-force are 37% and 50% greater on the variable-RPM rotor than the variable-pitch rotor. The 2/rev thrust oscillation is 12-13% of the mean rotor thrust, and is 6.5% lower for the variable-RPM rotor. The pitching and rolling moments are 11% and 9% smaller for the variable-RPM rotor, respectively.

At the aircraft level, the variable-RPM rotor has forces and moments acting at three distinct frequencies, because the rotors are spinning at different speeds, resulting in a beating phenomenon. The variable-pitch rotor sees vibration at only one frequency. The maximum amplitude of the vertical vibrations on the variable-RPM aircraft are similar in magnitude to the variable-pitch, assuming that the rotors on the latter are operating in-phase.

Author contact: Michael McKay (mckaym2@rpi.edu), Robert Niemiec (niemir@rpi.edu), Farhan Gandhi (fgandhi@rpi.edu)

ACKNOWLEDGMENTS

The authors would like to acknowledge the Department of Defense and the American Society of Engineering Education, for funding Mr. McKay and Mr. Niemiec through the National Defense Science and Engineering Graduate Fellowship.

REFERENCES

[1]N. Gupta, M. Kothari, and Abhishek, "Flight dynamics and nonlinear control design for variable pitch quadrotors," in *2016 American Control Conference*, ACC, July 6-8 2016.

[2]T. Pang, K. Peng, F. Lin, and B. M. Chen, "Towards long-endurance flight: Design and implementation of a variable-pitch gasoline engine quadrotor," in *12th IEEE International Conference on Control & Automation*, ICCA, June 1-3 2016.

[3]Abhishek, R. Gadekar, A. Duhoon, M. Kothari, and S. K. L. R. G. Suryavanshi, "Design, development, and closed-loop flight-testing of a single power plant variable pitch quadrotor unmanned aerial vehicle," in *American Helicopter Society 73nd Annual Forum, Fort Worth, TX*, AHS, May 2017.

[4]M. Cutler, N.-K. Ure, B. Michini, and J. How, "Comparison of fixed and variable pitch actuators for agile quadrotors," in *AIAA Guidance, Navigation, and Control Conference, Portland, OR*, AIAA, Aug. 2011.

[5]M. Cutler and J. P. How, "Analysis and control of a variable-pitch quadrotor for agile flight," *Journal of Dynamics Systems, Measurement, and Control*, vol. 137, pp. 101002–1–101002–14, October 2015.

[6]P. Pounds, R. Mahoney, P. Hynes, and J. Roberts, "Design of a four-rotor aerial robot," in *Australasian Conference on Robotics and Automation, Auckland, NZ*, Nov. 2002.

[7]M. Drela, "Qprop users guide." Online, http://web.mit.edu/drela/Public/web/qprop/, 2009.

[8]M. Cutler and J. How, "Actuator constrained trajectory generation and control for variable-pitch quadrotors," in *AIAA Guidance, Navigation, and Control, Minneapolis, MN*, Aug. 2012.

[9]M. Cutler, "Design and control of an autonomous variable-pitch quadrotor helicopter," mathesis, Massachusetts Institute of Technology, Sept. 2012.

[10]R. Niemiec and F. Gandhi, "Effects of inflow model on simulated aeromechanics of a quadrotor helicopter," in *American Helicopter Society 72nd Annual Forum, West Palm Beach, FL*, AHS, May 2016.

[11]D. A. Peters, D. D. Boyd, and C. J. He, "Finite-state induced-flow model for rotors in hover and forward flight," in *American Helicopter Society 43rd Annual Forum, St Louis, MO*, AHS, May 1987.

[12]R. Niemiec and F. Gandhi, "A comparison between quadrotor flight configurations," in *42nd Annual European Rotorcraft Forum, Lille, France*, ERF, Sept. 2016.